Monthly Notices
of the
ROYAL ASTRONOMICAL SOCIETY

MNRAS **548,** 1–10 (2026) https://doi.org/10.1093/mnras/stag744
Advance Access publication 2026 April 20

ExoMol photodissociation cross-sections – III. Temperature-dependent photodissociation and photoabsorption spectra for NH

Armando N. Perri,[1] Tereza Uhlíková,[2] Gap-Sue Kim,[3] Sergei N. Yurchenko[1] and Jonathan Tennyson[1★]

[1]*Department of Physics and Astronomy, University College London, WC1E 6BT London, UK*
[2]*Department of Analytical Chemistry, University of Chemistry and Technology, Technická 6, Prague, Czech Republic*
[3]*Dharma College, Dongguk University, 30, Pildong-ro 1-gil, Jung-gu, Seoul 04620, Korea*

Accepted 2026 April 16. Received 2026 April 16; in original form 2026 February 15

ABSTRACT

The photoabsorption of the imidogen (NH) radical is important in various astronomical and industrial processes. In particular, its photodissociation in the ultraviolet region is crucial for correct chemical modelling and dynamics. An updated spectroscopic model, named 2kNigHt, is presented for the 12 lowest electronic states of NH. This model is used to compute a new bound–bound line list up to 50 000 cm^{-1} for the four ^{14}N^{1}H, ^{14}N^{2}H, ^{15}N^{1}H, and ^{15}N^{2}H isotopologues. Temperature-dependent photoabsorption, continuum photoabsorption, and photodissociation cross-sections, as well as associated photolysis rates under several important radiation fields, are computed. These cross-sections cover wavelengths longer than the hydrogen Lyα line for temperatures up to 10 000 K. All results are made available in the ExoMol and ExoPhoto databases.

Key words: astrochemistry – molecular data – planets and satellites: atmospheres – stars: atmospheres – ISM: molecules.

1 INTRODUCTION

Imidogen (NH) is a highly reactive radical that is a transient species in many systems. Astronomically, NH has been detected in the interstellar medium (D. M. Meyer & K. C. Roth 1991; I. A. Crawford & D. A. Williams 1997; J. Cernicharo, J. R. Goicoechea & E. Caux 2000; T. Weselak et al. 2009; C. M. Persson et al. 2010, 2012), as well as in the atmosphere of the Sun (H. D. Babcock 1945; N. Grevesse et al. 1990), protostars (P. Hily-Blant et al. 2010), dwarfs (M. Spite et al. 2022), giants (C. Sneden 1973; V. V. Smith & D. L. Lambert 1986; W. Aoki & T. Tsuji 1997), supergiants (D. L. Lambert et al. 1984), and comets (P. Swings, C. T. Elvey & H. W. Babcock 1941; E. B. Hanten et al. 2025). It serves as an astronomical measure of nitrogen abundance that is independent of other non-hydrogen elements. Industrially, NH spectroscopy is prominent in air (S. S. Harilal, B. E. Brumfield & M. C. Phillips 2018) and liquid (R. Pflieger et al. 2017) plasma processes, where it is essential in ammonia monitoring (D. Zhang et al. 2019) and assists in wastewater purification (A. Hamdan, J.-L. Liu & M. S. Cha 2018). It is also observed in combustion and flash photolysis processes, in particular associated with the successive hydrogen abstraction of ammonia (P. Glarborg et al. 2018; C. Brackmann et al. 2018; N. Lamoureux, L. Gasnot & P. Desgroux 2019; B. Jin et al. 2022; S. Mashruk et al. 2023). NH is also relevant in ultracold molecular physics; it has been cooled in a magnetic trap (M. Kajita 2006; W. C. Campbell et al. 2007; L. M. C. Janssen, A. van der Avoird & G. C. Groenenboom 2013), decelerated using the Stark (S. Y. T. van de Meerakker et al. 2006) and Zeeman (V. Plomp et al. 2019) effects, and has been proposed as a candidate for laser cooling (D. Li & W. Bian 2021; N.-Z. Yan et al. 2021) due to its highly diagonal Franck–Condon factors.

The photoabsorption spectroscopy of NH is reasonably complex for a simple hydride and offers an insight into several photodissociative mechanisms. The lowest 12 electronic states of NH as considered in this study are shown in Fig. 1 with their associated dissociation products. In the ultraviolet region (above ∼25 000 cm^{-1}; shorter than ∼400 nm), the spectrum is dominated by overlapping direct photodissociative features from the $2\,^3\Sigma^-$ and $2\,^3\Pi$ repulsive electronic states at 120–160 nm. *Ab initio* cross-sections for these two processes were calculated at 0 K by K. P. Kirby & E. M. Goldfield (1991). There is also a continuum photoabsorption feature peaked at ∼300 nm from A $^3\Pi$ predissociation induced by the $1\,^5\Sigma^-$ repulsive state, which was suggested by W. H. Smith, J. Brzozowski & P. Erman (1976) and D. Patel-Misra et al. (1991) through lifetime analyses, and modelled without rotational structure by A. N. Heays, A. D. Bosman & E. F. van Dishoeck (2017). These *ab initio* cross-sections are collated in the Leiden photodissociation and photoionization database (A. N. Heays et al. 2017; H. R. Hrodmarsson & E. F. van Dishoeck 2023), in addition to a temperature-independent feature centred at 100 000 cm^{-1} (100 nm) to account for processes involving higher electronic states (R. Ghosh et al. 2025). From ExoMol (J. Tennyson et al. 2024), NH continuum photoabsorption has been studied by A. N. Perri & L. K. McKemmish (2024) and T. Uhlíková

★ E-mail: j.tennyson@ucl.ac.uk

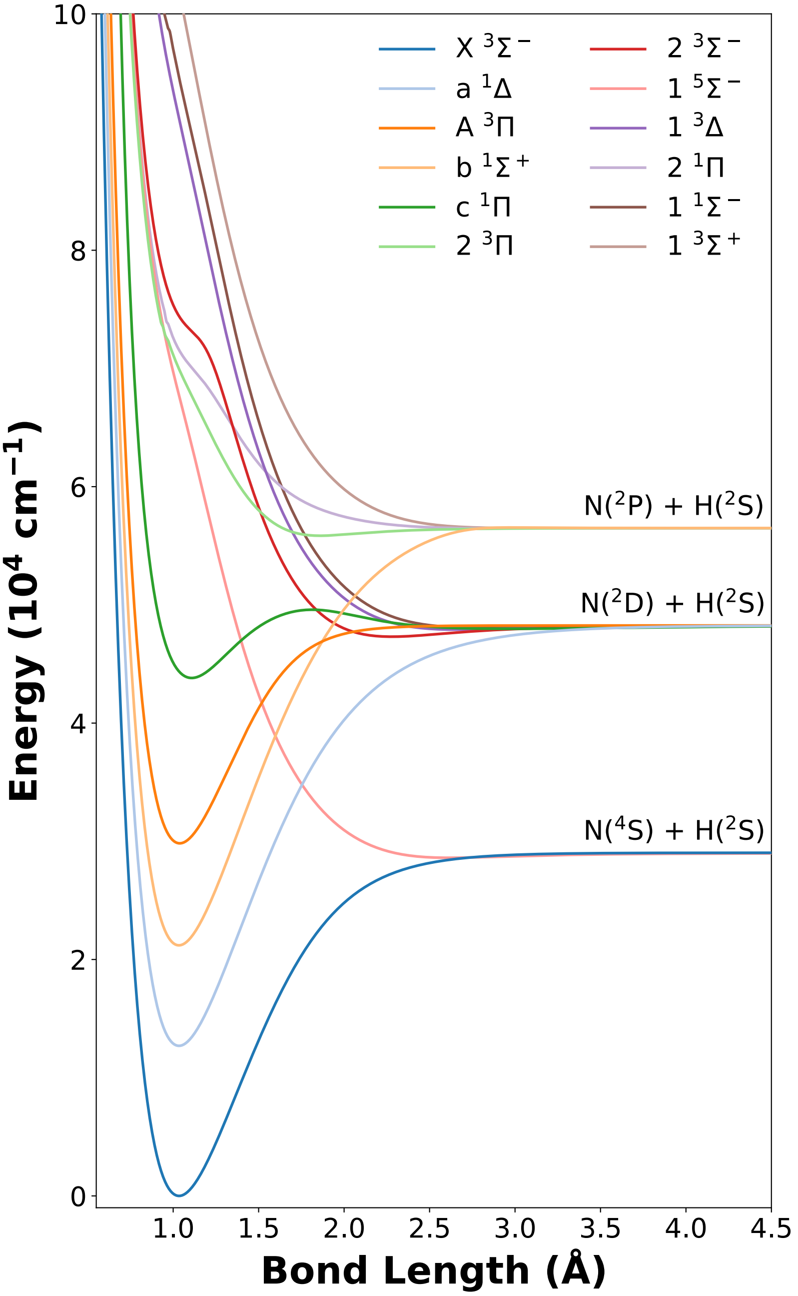

Figure 1. The lowest 12 potential energy curves of NH considered in this study with their associated dissociation products.

et al. (2025) through variational nuclear motion calculations using Duo (S. N. Yurchenko et al. 2016) and spectral post-processing using ExoCross (S. N. Yurchenko, A. F. Al-Refaie & J. Tennyson 2018).

The study of A. N. Perri & L. K. McKemmish (2024) considered the five lowest electronic states (X $^3\Sigma^-$, a $^1\Delta$, b $^1\Sigma^+$, A $^3\Pi$, and c $^1\Pi$) of NH. This involved construction of a spectroscopic model comprising *ab initio* potential energy, coupling (e.g. spin-orbit and angular momenta) and dipole moment curves. For the X $^3\Sigma^-$, a $^1\Delta$, and A $^3\Pi$ electronic states, the majority of these curves were refined to experimental energy levels from a previous MARVEL (Measured Active Rotational-Vibrational Energy Levels) study (D. Darby-Lewis et al. 2019) that considered high-resolution spectroscopy measurements from 18 publications (P. F. Bernath & T. Amano 1982; D. A. Ramsay & P. J. Sarre 1982; F. van den Heuvel, W. Meerts & A. Dymanus 1982; J. L. Hall et al. 1985; D. Boudjaadar et al. 1986; C. R. Brazier, R. S. Ram & P. F. Bernath 1986; K. R. Leopold, K. M. Evenson & J. M. Brown 1986; R. S. Ram & P. F. Bernath 1986; W. Ubachs et al. 1986; W. Hack & T. Mill 1990; M. Geller et al. 1991; T. Klaus, S. Takano & G. Winnewisser 1997; R. S. Ram, P. F. Bernath & K. H. Hinkle 1999; S. Y. T. van de Meerakker et al. 2003; J. Flores-Mijangos et al. 2004; F. Lewen et al. 2004; A. Robinson et al. 2007; R. S. Ram & P. F. Bernath 2010). Additional c $^1\Pi$ – a $^1\Delta$ transitions from W. R. M. Graham & H. Lew (1978) were subsequently added by T. Uhlíková et al. (2025). Hyperfine effects are largely unresolved in rovibronic spectra and were not considered in these studies. This model was then used to generate an accurate line list, given the name kNigHt, through rovibronic calculations in Duo. This ‘trihybrid’ line list includes energies obtained using three methodologies (L. K. McKemmish 2021; L. K. McKemmish et al. 2024); MARVEL experimental energies and effective Hamiltonian energies from J. S. A. Brooke et al. (2014), J. S. A. Brooke, P. F. Bernath & C. M. Western (2015), and A. M. Fernando et al. (2018) were explicitly included to ensure accuracy alongside the complementary completeness offered by the variational model. The kNigHt line list is applicable for high temperatures and covers wavenumbers up to 47 500 cm^{-1} (longer than ∼211 nm) for the ^{14}N^{1}H, ^{14}N^{2}H, ^{15}N^{1}H, and ^{15}N^{2}H isotopologues. These data have recently been used to successfully probe ^{14}N^{1}H/^{14}N^{2}H and ^{15}N^{1}H/^{14}N^{1}H ratios in several bright comets (E. B. Hanten et al. 2025), which exemplifies the utility of isotopologue extrapolation (L. K. McKemmish et al. 2024).

The study of T. Uhlíková et al. (2025) developed and tested a variety of techniques used to compute photodissociation cross-sections and, in particular, quasi-continuum properties (line positions, line widths, and lifetimes) for quasi-bound electronic states. The kNigHt spectroscopic model was employed with additional *ab initio* data for seven high-lying electronic states and a refined c $^{1}\Pi$ state. The new c $^{1}\Pi$ potential energy curve was necessary to correctly account for the shape resonance that is essential for its quasi-bound photoabsorption.

Consequently, this work extends these two studies to analyse temperature effects on the photoabsorption and photodissociation spectra of NH up to 10 000 K. Temperature-dependent cross-sections are generated for all important features with wavelengths longer than the hydrogen Lyα line at 121.6 nm. An updated spectroscopic model, given the name 2kNigHt, is produced to ensure a self-consistent line list, primarily for the quasi-bound c $^{1}\Pi$ state. This article is thus structured as follows: the methodologies associated with the spectroscopic model and high-resolution bound–bound line list, as well as for the calculation of temperature-dependent cross-sections and photolysis rates, are overviewed in Section 2. The results are then presented in Section 3 for the ^{14}N^{1}H, ^{14}N^{2}H, ^{15}N^{1}H, and ^{15}N^{2}H isotopologues and conclusions in Section 4.

2 METHODOLOGY

This work builds on the initial kNigHt spectroscopic model of A. N. Perri & L. K. McKemmish (2024) supplemented by the *ab initio* and fitted c $^{1}\Pi$ curves of T. Uhlíková et al. (2025). Due to the various couplings that link all five electronic states considered in kNigHt, however, direct combination of these sources leads to deviations in the rovibronic energy residuals compared to the MARVEL experimental data. For this reason, a refit was necessary to produce an updated self-consistent spectroscopic model named 2kNigHt. All couplings to the seven higher electronic states given by T. Uhlíková et al. (2025) were introduced. This new model facilitates calculation of temperature-dependent continuum photoabsorption and photodissociation cross-sections, as well as associated rates, for all processes down to 121.6 nm.

2.1 Spectroscopic model and line list

The original kNigHt spectroscopic model considered the lowest five electronic states (X $^{3}\Sigma^{-}$, a $^{1}\Delta$, b $^{1}\Sigma^{+}$, A $^{3}\Pi$, and c $^{1}\Pi$) of NH. Notably, the potential energy curve (PEC) of the quasi-bound c $^{1}\Pi$ state was simply included as *ab initio* grid points. This curve has a small barrier above its dissociation asymptote, which was subsequently fit by T. Uhlíková et al. (2025) with the two-state diabatic analytic model (S. N. Yurchenko et al. 2024) given by

$$\mathbf{A} = \begin{pmatrix} V_1(R) & V_{12}(R) \\ V_{12}(R) & V_2(R) \end{pmatrix}. \tag{1}$$

For the lower bound diabatic $V_1(R)$ curve, an extended Morse oscillator (EMO) function was used as given by

$$V_1(R) = \mathrm{T_e} + \mathrm{D_e}\left[1 - \exp\left(-\sum_{i=0}^{N} b_i \xi_4^i (R - R_e)\right)\right]^2, \tag{2}$$

where $\mathrm{T_e}$ is the term energy, $\mathrm{D_e}$ is the dissociation energy, $\mathrm{R_e}$ is the equilibrium bond length, and $\{b_i\}$ are vibrational fitting parameters. The Šurkus variable of order p is

$$\xi_p = \frac{R^p - R_e^p}{R^p + R_e^p}. \tag{3}$$

For the upper repulsive diabatic $V_2(R)$ curve, an inverse polynomial was used as given by

$$V_2(R) = A_e + \frac{b_6}{R^6}, \tag{4}$$

where A_e is the dissociation asymptote and b_6 is a fitting parameter. There is no curve in the *ab initio* study that corresponds to $V_2(R)$. The upper curve obtained from diagonalizing equation (1) is therefore not of physical significance.

For the off-diagonal diabatic $V_{12}(R)$ curve, an inverted EMO PEC with an asymptote of zero as $R \to \infty$ was used as given by

$$V_{12}(R) = W_e\left[1 - \left[1 - \exp\left(-\sum_{i=0}^{N} b_i \xi_4^i (R - R_e)\right)\right]^2\right]. \tag{5}$$

The final c $^{1}\Pi$ adiabatic potential energy curve is then constructed as the lower eigenvalue of the diabatic matrix **A** and the upper component is disregarded.

Born-Oppenheimer breakdown (BOB) and Λ-doubling (λ_q) interactions have also been included for the c $^{1}\Pi$ state. The former allows for an empirical position-dependent variation of the rotational mass (R. J. Le Roy & Y. Huang 2002; R. P. Brady et al. 2024), which is known to be important for electronic centrifugal distortion in hydrides with large rotational constants, seen for NH itself (M. Melosso et al. 2019), HF (R. J. Le Roy 1999), and MgH (R. D. E. Henderson et al. 2013).

The potential energy and coupling curves associated with the additional seven excited electronic states considered by T. Uhlíková et al. (2025) were further added to the 2kNigHt spectroscopic model. The *ab initio* permanent (diagonal) and transition (off-diagonal) dipole moment curves were also included, which were each fit to the irregular functional form suggested by E. S. Medvedev & V. G. Ushakov (2022). It was further important to morph the *ab initio* potential energy curves at large bond lengths to ensure the correct dissociation asymptote for each channel. This was achieved using

$$V_{\mathrm{morphed}}(R) = V_{abinitio}(R) f(R) + A_e\left[1 - f(R)\right] \tag{6}$$

with

$$f(R) = \frac{1}{2}\left[1 - \tanh(a\xi_4)\right], \tag{7}$$

where $a = 5.0$ and $R_e = 2.75$ Å for the b $^{1}\Sigma^{+}$ electronic state, and $a = 2.0$ and $R_e = 2.50$ Å for the other states.

Upon solution of the time-independent nuclear Schrödinger equation in Duo, rovibronic states are characterized as either bound or unbound. These are separated based on two criteria; first, the density ρ_i of each wavefunction Ψ_i is checked for asymptotic behaviour in a small region δ at the outer box length R_{outer} as

$$\rho_i = \int_{R_{\text{outer}}-\delta}^{R_{\text{outer}}} |\Psi_i|^2 dR. \tag{8}$$

Unbound states belonging to the continuum have non-zero density in this outer region and can thus be differentiated from the bound states of each potential well. Secondly, the expectation value of bond length is calculated for each state as

$$\langle R\rangle_i = \int_{R_{\text{inner}}}^{R_{\text{outer}}} |\Psi_i|^2 R dR. \tag{9}$$

This value is physically meaningful and helps to better distinguish between quasi-bound and unbound states, where the former may still possess some asymptotic behaviour far from equilibrium.

2.2 Cross-sections

ExoCross (S. N. Yurchenko et al. 2018) was used to generate cross-sections from the 2kNigHt line list. For a transition between initial i and final f discrete states, the line intensity is given by

$$I_{fi} = \frac{g_f^{\text{tot}} A_{fi}}{8\pi c \tilde{\nu}_{fi}^2} \frac{e^{-c_2 \tilde{E}_i/T}\left(1 - e^{-c_2 \tilde{\nu}_{fi}/T}\right)}{Q(T)}, \tag{10}$$

where $g^{\text{tot}} = g^{\text{ns}}(2J+1)$ is the total degeneracy factor, g^{ns} is the nuclear spin statistical weight factor, A_{fi} is the Einstein A coefficient (s^{-1}), $\tilde{\nu}_{fi}$ is the transition frequency (cm^{-1}), $\tilde{E}$ is energy (cm^{-1}), T is temperature (K) and $Q(T)$ is the partition function expressed as

$$Q(T) = \sum_n g_n^{\text{tot}} e^{-hc\tilde{E}_n/k_B T}. \tag{11}$$

The total lifetime τ_{tot} broadening of each line results from both radiative τ_{rad} and predissociative $*\tau_{\text{pre}}$ contributions with

$$\frac{1}{\tau_{\text{tot}}} = \frac{1}{\tau_{\text{rad}}} + \frac{1}{\tau_{\text{pre}}}. \tag{12}$$

This yields a Lorentzian broadening profile given by

$$g_L(\tilde{\nu}) = \frac{1}{\pi} \frac{\Gamma_L/2}{(\tilde{\nu} - \tilde{\nu}_0)^2 + (\Gamma_L/2)^2}, \tag{13}$$

with full-width at half-maximum of

$$\Gamma_L = \frac{1}{2\pi c \tau_{\text{tot}}}. \tag{14}$$

The radiative lifetimes τ_{rad} are calculated through summation of Einstein A_{if} coefficients over all transitions from a given state i to final states f as

$$\tau_{\text{rad}} = \frac{1}{\sum_{i<f} A_{if}} \tag{15}$$

For quasi-bound states, the predissociative lifetimes τ_{pre} were determined using the stabilization methodology involving repeated calculations as a function of R_{outer}. This procedure is outlined by A. U. Hazi & H. S. Taylor (1970), V. A. Mandelshtam, T. R. Ravuri & H. S. Taylor (1993), Z. Bacic & J. Simons (1982), and has been employed by G. B. Mitev, S. N. Yurchenko & J. Tennyson (2024), T. Uhlíková et al. (2025), and A. Sokolov et al. (2025).

The additional temperature-dependent Doppler line broadening is described by a Gaussian profile. The final cross-section is given as the sum over all lines broadened by their respective Lorentzian and Gaussian contributions. This treatment is appropriate for bound–bound transitions stored in the 2kNigHt line list. In the variational approach developed by M. Pezzella, S. N. Yurchenko & J. Tennyson (2021) and applied by M. Pezzella, S. N. Yurchenko & J. Tennyson (2022), and G. B. Mitev et al. (2025), repulsive electronic states are treated equivalently to bound states in the solution of the time-independent nuclear Schrödinger equation within a finite region. This leads to a sampling of the continuum, where line positions from repulsive states are dependent on the radial box size of the calculation. It is thus necessary to broaden each continuum line with some artificial profile to generate a continuous spectrum. As detailed extensively by T. Uhlíková et al. (2025), and G. B. Mitev et al. (2025), a robust broadening scheme is realized using a 'particle-in-a-box' model. This treatment utilizes a variable Gaussian full-width at half-maximum dependent on the energy level separation for the chosen radial box size.

2.3 Photolysis rates

The temperature-dependent photolysis rate of a dissociative process is given by

$$k(T) = \int_{\lambda_i}^{\lambda_f} F(\lambda)\sigma(\lambda, T) d\lambda, \tag{16}$$

where λ is wavelength (nm), T is the molecular temperature (K), $F(\lambda)$ is the photon flux (photons s^{-1} cm^{-2} nm^{-1}), and $\sigma(\lambda, T)$ is the temperature-dependent photodissociation cross-section (cm^2 molecule^{-1}). This equation assumes that all transitions in the wavelength region of interest between λ_i and λ_f lead to photolysis, although dissociation into a particular product channel may be accounted for using partial cross-sections (R. J. Pattillo et al. 2018; G. B. Mitev et al. 2025; A. Sokolov, S. N. Yurchenko & J. Tennyson 2026).

All photolysis rates are crucially dependent on the photon flux $F(\lambda)$ radiated upon the molecules in a system. This work considers rates under the interstellar radiation field (ISRF) (B. T. Draine 1978; E. F. van Dishoeck & J. H. Black 1982) and model blackbody (BB) radiation fields at 4000, 10 000, and 20 000 K. The model BB fluxes are particularly useful for exoplanetary studies to gauge the variability of molecular photodissociation over a range of stellar temperatures. Additionally, in all subsequent analysis, the integrated energy intensity of each field is scaled to match that of the ISRF in the 91.2–200 nm region (2.6×10^{-10} W cm^{-2}) (A. N. Heays et al. 2017; H. R. Hrodmarsson & E. F. van Dishoeck 2023; M. Pezzella et al. 2022).

3 RESULTS

3.1 Spectroscopic model and line list

The 2kNigHt spectroscopic model with all fitted parameters is given in the 14-H__2kNigHt.model Duo input file available in supplementary materials. The new 2kNigHt line list includes all bound energy levels, notably introducing $v = 2$ quasi-bound levels for the c $^1\Pi$ electronic state. The bound state selection thresholds were chosen to be $\rho < 0.05$ and $\langle R\rangle < 3.0$ Å. The Duo

Table 1. The root mean square error (cm^{-1}) within each vibronic level in the kNigHt (A. N. Perri & L. K. McKemmish 2024), JCP (T. Uhlíková et al. 2025), and 2kNigHt (this work) energy levels compared to the MARVEL experimental data. The number of states N_{states} within each vibronic level is given in the final rows.

Line list	v	$\mathrm{X}\,^3\Sigma^-$	$\mathrm{a}\,^1\Delta$	$\mathrm{A}\,^3\Pi$	$\mathrm{c}\,^1\Pi$
kNigHt	0	0.165	0.013	0.065	0.900
	1	0.223	0.018	0.045	12.046
	2	0.177	0.044	0.034	
	3	0.028	0.049		
	4	0.087			
	5	0.062			
	6	0.175			
	All	0.154	0.029	0.053	3.583
	N_{states}	541	110	402	24
JCP	0				0.360
	1				0.218
	2				2.288
	All				0.711
	N_{states}				63
2kNigHt	0	0.117	0.016	0.141	0.123
	1	0.103	0.021	0.052	0.094
	2	0.096	0.049	0.029	2.346
	3	0.047	0.070		
	4	0.070			
	5	0.045			
	6	0.112			
	All	0.091	0.036	0.101	0.777
	N_{states}	541	110	403	65

Table 2. A summary of the four 2kNigHt isotopologue line lists.

Isotopologue	g^{ns}	J_{max}	N_{states}	$N_{\mathrm{transitions}}$
$^{14}\mathrm{N}^1\mathrm{H}$	6	58	4552	236 012
$^{14}\mathrm{N}^2\mathrm{H}$	9	80	8575	618 747
$^{15}\mathrm{N}^1\mathrm{H}$	4	58	4561	237 321
$^{15}\mathrm{N}^2\mathrm{H}$	6	80	8626	623 576

calculation employed 7501 sinc functions in a discrete variable representation (DVR), which are uniformly distributed for bond lengths $R = 0.5 - 8.0$ Å. The lowest 150 vibrational basis functions of each electronic state were retained.

The root mean square error within each vibronic level are presented in Table 1 as compared to the MARVEL experimental energy levels (D. Darby-Lewis et al. 2019) for the kNigHt and 2kNigHt line lists, as well as for the $\mathrm{c}\,^1\Pi$ model of T. Uhlíková et al. (2025). It can be seen that the 2kNigHt line list is of similar accuracy to the previous data in light of the additional 31 coupling curves added. It is hence expected that the 2kNigHt line list can more accurately predict bound energy levels up to 50 000 cm^{-1}. The assignment of non-rigorous quantum numbers (notably v and N for triplet states) close to dissociation is still unreliable and should be treated as a best estimate. Additionally, the 2kNigHt model provides improved transition intensities due to correct wavefunction mixing from the introduced coupling curves, which were checked for phase consistency.

In the bound–bound region set here below 50 000 cm^{-1}, the $\mathrm{b}\,^1\Sigma^+$ electronic state is still modelled with only *ab initio* curves. A. Gilles, J. Masanet & C. Vermeil (1974) and J. Masanet, A. Gilles & C. Vermeil (1974) measured the $\mathrm{b}\,^1\Sigma^+ - \mathrm{X}\,^3\Sigma^-$ band near 471 nm with $\nu_{00} \approx 21\,237$ cm^{-1}. The *ab initio* potential energy curve was shifted in this work to match this result. The opacity contribution is still described sufficiently due to lack of any significant couplings.

The predissociative lifetimes were determined here using the stabilization methodology for 2 001 individual calculations. The outer sinc-DVR box length was varied from 6 to 8 Å and an inner sinc-DVR box length fixed at 0.5 Å. The Lorentzian distribution in equation (13) was fit to a histogram of energies constructed with 199 bins over a $\pm 3\sigma$ range about the mean value. This yields the full-width at half-maximum Γ_L for each rovibronic state such that predissociative lifetimes and rates can be calculated. These were computed for $\mathrm{A}\,^3\Pi$ and $\mathrm{c}\,^1\Pi$ rovibronic states categorized as bound using ρ and $\langle R \rangle$, and with $3\sigma > 10^{-6}$ cm^{-1}.

The new 2kNigHt spectroscopic model also allows for more useful predictions for the $^{14}\mathrm{N}^2\mathrm{H}$, $^{15}\mathrm{N}^1\mathrm{H}$, and $^{15}\mathrm{N}^2\mathrm{H}$ minor isotopologues, however, caution is advised due to the mass-dependent BOB curve used. Nevertheless, A. N. Perri & L. K. McKemmish (2024) showed that the original kNigHt line list can predict rovibrational transitions to better than 1 cm^{-1} for each isotopologue as compared to lines collated by M. Melosso et al. (2019). Energy uncertainties and isotopologue extrapolation were calculated as described by L. K. McKemmish et al. (2024). Additionally, for minor isotopologues, only the radiative contribution of the lifetime was included in the final line lists.

A summary of the four 2kNigHt isotopologue line lists presented in this work is given in Table 2. These line lists are available in the ExoMol database in the form of individual.states and.trans files, which are identical in format to those of A. N. Perri & L. K. McKemmish (2024).

3.2 Cross-sections

The main result of this work is a set of temperature-dependent (up to 10 000 K) photoabsorption, continuum photoabsorption, and photodissociation cross-sections for the main $^{14}\mathrm{N}^1\mathrm{H}$ isotopologue. The bound–bound contribution of the photoabsorption cross-sections can be produced from the 14N-1H__2kNigHt.states and 14N-1H__2kNigHt.trans files. For 40 selected temperatures, the continuum photoabsorption (bound–continuum contribution) and photodissociation cross-sections are available in the ExoMol (J. Tennyson et al. 2024) and ExoPhoto (Q.-H. Ni et al. 2025) databases, respectively.

The photoabsorption cross-sections include all bound–bound transitions with Doppler and lifetime broadening, as well as the bound–continuum contribution. The $^{14}\mathrm{N}^1\mathrm{H}$ photoabsorption cross-sections for selected temperatures are shown in Fig. 2. The continuum photoabsorption cross-sections only include the bound–continuum contribution, which are provided on a 0.01 cm^{-1} wavenumber grid. An example extract at 3000 K is given in Table 3.

The photodissociation cross-sections include the bound–continuum contribution in addition to quasi-bound features scaled by their dissociation efficiency η_{diss}. This efficiency is taken as

$$\eta_{\mathrm{diss}} = \frac{k_{\mathrm{pre}}}{k_{\mathrm{rad}} + k_{\mathrm{pre}}} = \frac{\tau_{\mathrm{rad}}}{\tau_{\mathrm{rad}} + \tau_{\mathrm{pre}}}, \tag{17}$$

which models the competition between radiative decay with rate $k_{\mathrm{rad}} = 1/\tau_{\mathrm{rad}}$ and predissociation with rate $k_{\mathrm{pre}} = 1/\tau_{\mathrm{pre}}$. The photodissociation cross-sections are provided on a 0.1 nm wavelength grid. An example extract at 3000 K is given in Table 4.

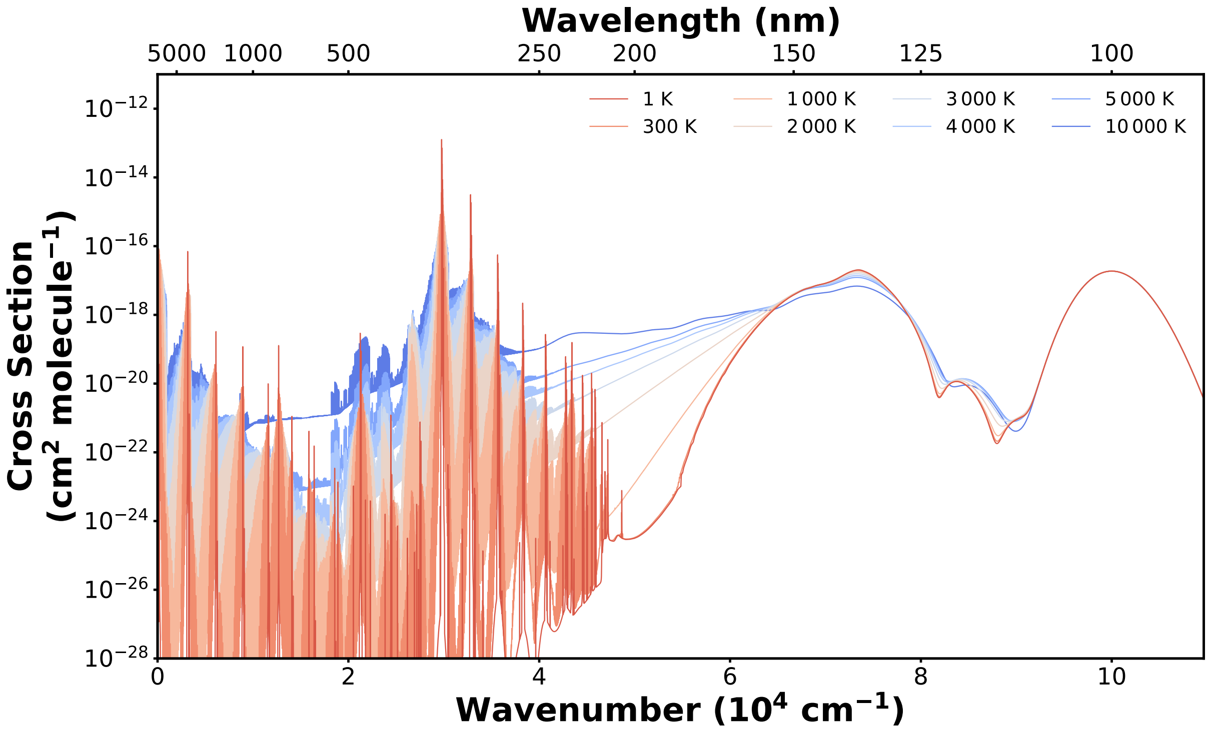

Figure 2. Temperature-dependent photoabsorption cross-sections for ^{14}N^{1}H computed using the 2kNigHt spectroscopic model with inclusion of the additional Leiden feature at 100 nm. These include all bound–bound transitions with both Doppler and lifetime broadening, as well as the bound–continuum contribution.

Table 3. An extract of the 2kNigHt continuum photoabsorption cross-section at 3000 K on a 0.01 cm^{-1} wavenumber grid for 0–109 650 cm^{-1}.

Wavenumber (cm^{-1})	Cross-section (cm^2 molecule^{-1})
0.000 0000E+00	4.421 2968E−28
1.000 0000E−02	4.422 0995E−28
2.000 0000E−02	4.422 9022E−28

Table 4. An extract of the 2kNigHt photodissociation cross-section at 3000 K on a 0.1 nm wavelength grid for 91.2–1 000 000 nm.

Wavelength (nm)	Cross-section (cm^2 molecule^{-1})
9.120 0000E+01	1.862 3383E−21
9.130 0000E+01	4.255 2227E−21
9.140 0000E+01	5.155 0419E−21

Specifically, NH photodissociation in this work arise primarily from direct dissociation via excitation into the repulsive 2 $^3\Sigma^-$ and 2 $^3\Pi$ electronic states, A $^3\Pi$ predissociation induced by spin–orbit coupling to the 1 $^5\Sigma^-$ repulsive state, and c $^1\Pi$ tunnelling.

Direct NH photodissociation via the 2 $^3\Sigma^-$ and 2 $^3\Pi$ repulsive states produces a broad feature in the 50 000–85 000 cm^{-1} region. The temperature-dependent photodissociation cross-sections associated with these overlapping features are shown in Fig. 3. The partial 2 $^3\Sigma^-$ and 2 $^3\Pi$ contributions at 300 K, as well as comparisons to K. P. Kirby & E. M. Goldfield (1991) at 0 K, were provided by T. Uhlíková et al. (2025).

A $^3\Pi$ predissociation induced by the 1 $^5\Sigma^-$ repulsive state is an important mechanism to consider as the A $^3\Pi$ – X $^3\Sigma^-$ electronic transition dominates the ultraviolet spectrum at ∼300 nm. The line positions and intensities for this feature are well described by the kNigHt spectroscopic model of A. N. Perri & L. K. McKemmish (2024). The lifetimes, however, were only calculated for the radiative contribution, such that any subsequent line broadening does not account for predissociative effects. Consequently, these were updated using predissociative lifetimes from stabilization calculations. These are shown in Fig. 4 with the semi-classical results of D. Patel-Misra et al. (1991) and R. S. da Silva et al. (2026). The progression for small N is consistent with D. Patel-Misra et al. (1991) for $v = 0$, 1, and 2, however, deviates for large N. The $N = 0$ results are mostly consistent with R. S. da Silva et al. (2026) for high v. The total lifetime τ_{tot} was then used to broaden each line with Lorentzian profiles. It should be noted that the total lifetime τ_{tot} is now given in the 14-H__2kNigHt.states file, which allows both radiative and predissociative lifetime broadening effects to be included when generating cross-sections from the line list (J. Tennyson et al. 2023).

The photoabsorption and photodissociation cross-sections in the 25 000–40 000 cm^{-1} region for selected temperatures are presented in Fig. 5. These are dominated by the A $^3\Pi$ – X $^3\Sigma^-$ band system. The A $^3\Pi$ photoabsorption and photodissociation cross-sections of the Leiden database (A. N. Heays et al. 2017; H. R. Hrodmarsson & E. F. van Dishoeck 2023) are also shown in Fig. 5. The three photoabsorption band origins are all shifted by approximately 1630 cm^{-1} for an unclear reason. It is possible that the Leiden frequencies were selected to model the rotational distribution with a single Gaussian or miscalculated given that the shift is close to the zero-point energy of 1622 cm^{-1} with anharmonic correction from K. P. Huber & G. Herzberg (1979). Despite this, the Leiden database is targeted towards interstellar studies, where the ISRF is approximately constant such that shifts

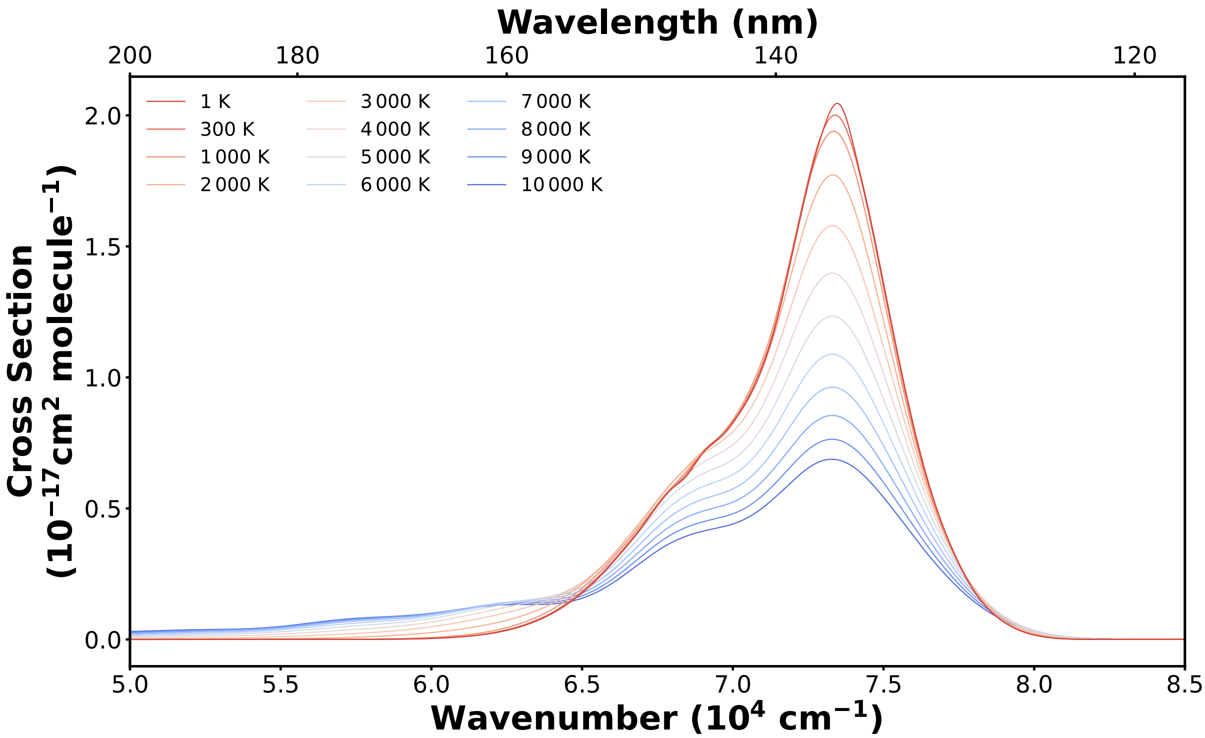

Figure 3. Temperature-dependent 2 $^3\Sigma^-$ and 2 $^3\Pi$ photodissociation cross-sections for ^{14}N^{1}H computed using the 2kNigHt spectroscopic model.

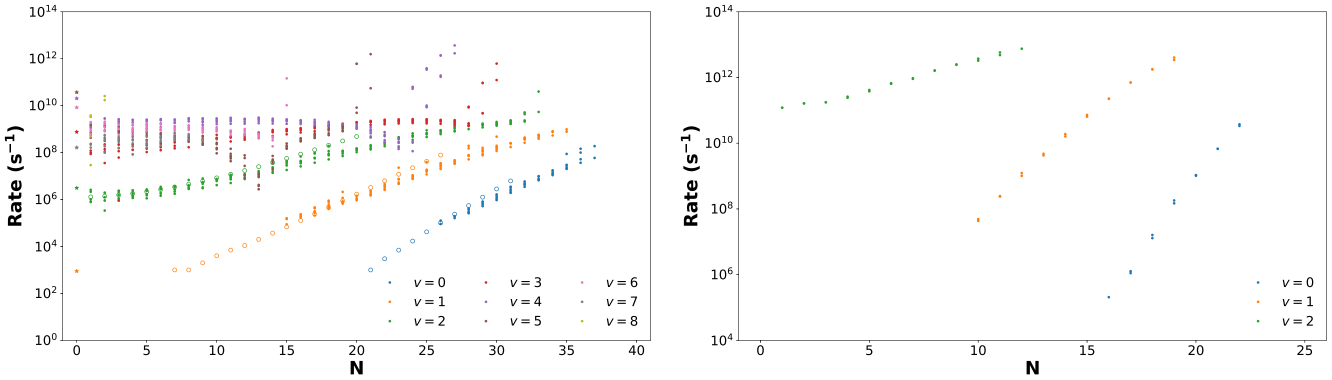

Figure 4. Predissociation rates calculated for A $^3\Pi$ (left) and c $^1\Pi$ (right) rovibronic states using the 2kNigHt spectroscopic model. The open circles and stars indicate the semiclassical A $^3\Pi$ rates of D. Patel-Misra et al. (1991) and R. S. da Silva et al. (2026), respectively.

in line position have a negligible impact on the overall photolysis rate.

The quasi-bound c $^1\Pi$ state also exhibits predissociation by direct tunnelling through its potential shape resonance. This mechanism is discussed extensively by T. Uhlíková et al. (2025). The updated predissociative rates calculated in this work are shown in Fig. 4.

3.3 Photolysis rates

The Leiden database provides photolysis rates for NH that arise from the direct 2 $^3\Sigma^-$ and 2 $^3\Pi$ photodissociation features, as well as from A $^3\Pi$ predissociation and an additional temperature-independent feature centred at 100 000 cm^{-1} (100 nm). These are calculated under various astronomical radiation fields. For the ^{14}N^{1}H 2kNigHt photodissociation cross-sections, temperature-dependent photolysis rates are given in Table 5 under the interstellar (ISRF) and BB radiation fields at 4000, 10 000, and 20 000 K. These rates include the additional feature at 100 nm from the Leiden database, and can thus be compared directly to A. N. Heays et al. (2017). It should again be noted that the integrated energy intensity of each field is scaled to match that of the ISRF in the 91.2–200 nm region (2.6×10^{-10} W cm^{-2}) (A. N. Heays et al. 2017; H. R. Hrodmarsson & E. F. van Dishoeck 2023; M. Pezzella et al. 2022).

Table 5 shows that the photolysis rates under the ISRF and 20 000 K BB are approximately constant across all molecular temperatures. There is a three-fold increase under the 10 000 K BB

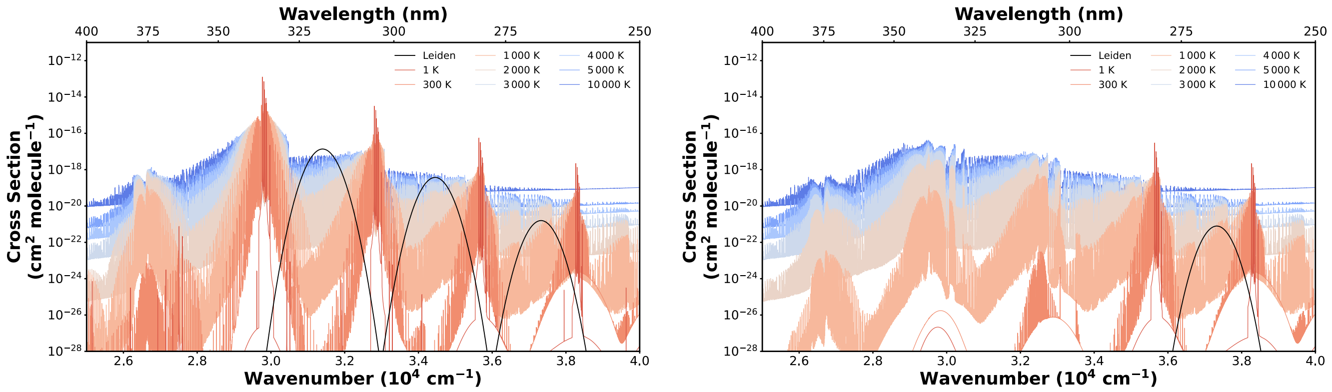

Figure 5. Temperature-dependent photoabsorption (left) and photodissociation (right) cross-sections for $^{14}N^1H$ in the 25 000–40 000 cm^{-1} region computed using the 2kNigHt line list. The spectra are dominated by the A $^3\Pi$ – X $^3\Sigma^-$ band system. The cross-sections from the Leiden database (A. N. Heays et al. 2017; H. R. Hrodmarsson & E. F. van Dishoeck 2023) are also shown. All lines in the photodissociation cross-sections (right) are scaled by their dissociation efficiency to give only the dissociative contribution from predissociation.

Table 5. Temperature-dependent photolysis rates (s^{-1}) for $^{14}N^1H$ under several fluxes below hydrogen ionization, including the temperature-independent feature centred at 100 nm from the Leiden database.

T_{mol} (K)	$F(\lambda) = 1$	ISRF	4000 K BB	10 000 K BB	20 000 K BB
1	3.40×10^{-16}	5.97×10^{-10}	2.56×10^{-11}	2.82×10^{-10}	5.38×10^{-10}
10	3.40×10^{-16}	5.97×10^{-10}	2.56×10^{-11}	2.82×10^{-10}	5.38×10^{-10}
100	3.40×10^{-16}	5.97×10^{-10}	2.48×10^{-11}	2.82×10^{-10}	5.39×10^{-10}
200	3.40×10^{-16}	5.97×10^{-10}	2.53×10^{-11}	2.83×10^{-10}	5.39×10^{-10}
300	3.40×10^{-16}	5.97×10^{-10}	2.59×10^{-11}	2.83×10^{-10}	5.39×10^{-10}
400	3.40×10^{-16}	5.97×10^{-10}	2.66×10^{-11}	2.83×10^{-10}	5.39×10^{-10}
500	3.40×10^{-16}	5.97×10^{-10}	2.78×10^{-11}	2.84×10^{-10}	5.39×10^{-10}
600	3.40×10^{-16}	5.97×10^{-10}	3.07×10^{-11}	2.84×10^{-10}	5.39×10^{-10}
700	3.40×10^{-16}	5.97×10^{-10}	3.73×10^{-11}	2.84×10^{-10}	5.39×10^{-10}
800	3.40×10^{-16}	5.97×10^{-10}	5.09×10^{-11}	2.85×10^{-10}	5.39×10^{-10}
900	3.40×10^{-16}	5.97×10^{-10}	7.63×10^{-11}	2.85×10^{-10}	5.39×10^{-10}
1000	3.39×10^{-16}	5.96×10^{-10}	1.20×10^{-10}	2.86×10^{-10}	5.39×10^{-10}
1500	3.38×10^{-16}	5.93×10^{-10}	9.72×10^{-10}	2.93×10^{-10}	5.37×10^{-10}
2000	3.37×10^{-16}	5.89×10^{-10}	3.82×10^{-9}	3.08×10^{-10}	5.34×10^{-10}
3000	3.33×10^{-16}	5.81×10^{-10}	1.72×10^{-8}	3.71×10^{-10}	5.28×10^{-10}
4000	3.30×10^{-16}	5.72×10^{-10}	3.75×10^{-8}	4.60×10^{-10}	5.20×10^{-10}
5000	3.25×10^{-16}	5.60×10^{-10}	5.97×10^{-8}	5.51×10^{-10}	5.10×10^{-10}
6000	3.20×10^{-16}	5.46×10^{-10}	8.10×10^{-8}	6.31×10^{-10}	4.97×10^{-10}
7000	3.14×10^{-16}	5.30×10^{-10}	1.01×10^{-7}	6.96×10^{-10}	4.83×10^{-10}
8000	3.08×10^{-16}	5.15×10^{-10}	1.20×10^{-7}	7.48×10^{-10}	4.68×10^{-10}
9000	3.02×10^{-16}	5.00×10^{-10}	1.39×10^{-7}	7.88×10^{-10}	4.55×10^{-10}
10 000	2.97×10^{-16}	4.86×10^{-10}	1.57×10^{-7}	8.20×10^{-10}	4.43×10^{-10}
Leiden	3.29×10^{-16}	5.75×10^{-10}	1.07×10^{-11}	2.41×10^{-10}	5.08×10^{-10}

towards higher temperatures, and an increase in four orders of magnitude under the 4000 K BB. The greatest increase in the photolysis rate with molecular temperature is thus expected for systems exposed to cool stellar radiation fields. This is due to the significant increase in the photodissociation cross-section below the first dissociation limit with molecular temperature, where variation in the initial rovibrational population shifts the cross-section towards lower frequencies into spectral regions where cooler BB fields peak in intensity. Consequently, the temperature-dependent photolysis rates presented here will substantially alter chemical models that involve NH photodissociation and its subsequent reaction pathways.

4 CONCLUSIONS

A complete set of temperature-dependent (up to 10 000 K) photoabsorption, continuum photoabsorption, and photodissociation spectra has been generated for NH for wavelengths above the hydrogen ionization limit (above 91.2 nm; below ∼109 650 cm^{-1}). This involved consolidation of the original five-state kNigHt spectroscopic model and subsequent cross-section and rate calculations using *ab initio* curves for seven additional high-lying repulsive states. Updated bound–bound line lists below 50 000 cm^{-1} have been presented for the four $^{14}N^1H$, $^{14}N^2H$, $^{15}N^1H$, and $^{15}N^2H$ isotopologues, with both predissociative and radiative contributions to the total lifetime now included for the main isotopologue. These line lists will help to improve characterization of isotopic ratios in a variety of astronomical and industrial systems.

This work now provides a comprehensive description of NH spectroscopy for wavelengths longer than the hydrogen Lyα line. Future improvements can always aim to refine the spectroscopic model upon the availability of new experimental data (e.g. line positions, line intensities, and lifetimes). Despite this, for NH photodissociation in the ultraviolet region, the temperature effects considered in this work are a major improvement over previous studies. This will aid chemical modelling and radiative transfer analyses for systems where NH is an important transient species.

The ExoMol photodissociation series provides temperature-dependent cross-sections for several diatomic molecules, namely, HCl, HF (M. Pezzella et al. 2022), OH (G. B. Mitev et al. 2025), NH, and CH (A. Sokolov et al. 2025). Future work will include the treatment of more complex diatomic molecules, such CN and SO, as well as triatomic molecules, including H_2O and H_2S. The trends observed for these diatomics will be expounded upon in a further study with recommendations for *a priori* temperature-dependent predictions. Additionally, the Duo nuclear motion programme is currently being extended to allow for the treatment of hyperfine effects in molecules with two non-zero nuclear spins such as $^{14}N^{1}H$.

ACKNOWLEDGEMENTS

This work was supported by the European Research Council (ERC) under the European Union's Horizon 2020 research and innovation programme through Advance Grant number 883830, STFC grant UKRI/ST/B001183/1, and STFC grant ST/Y001508/1. Computational resources were provided by the e-INFRA CZ project (ID:90254), supported by the Ministry of Education, Youth and Sports of the Czech Republic.

DATA AVAILABILITY

The 2kNigHt spectroscopic model (14N-1H__2kNigHt.model) is available in the supplementary material of this paper. The 2kNigHt isotopologue line lists, as well as the temperature-dependent continuum photoabsorption and photodissociation cross-sections for the $^{14}N^{1}H$ isotopologue, can be found in the ExoMol and ExoPhoto databases (www.exomol.com).

REFERENCES

Aoki W., Tsuji T., 1997, A&A, 328, 175

Babcock H. D., 1945, ApJ, 102, 154

Bacic Z., Simons J., 1982, J. Phys. Chem., 86, 1192

Bernath P. F., Amano T., 1982, J. Mol. Spectrosc., 95, 359

Boudjaadar D., Brion J., Chollet P., Guelachvilli G., Vervloet M., 1986, J. Mol. Spectrosc., 119, 352

Brackmann C., Nilsson E. J., Nauclér J. D., Aldén M., Konnov A. A., 2018, Combust. Flame, 194, 278

Brady R. P., Yurchenko S. N., Tennyson J., Kim G.-S., 2024, MNRAS, 527, 6675

Brazier C. R., Ram R. S., Bernath P. F., 1986, J. Mol. Spectrosc., 120, 381

Brooke J. S. A., Bernath P. F., Western C. M., van Hemert M. C., Groenenboom G. C., 2014, J. Chem. Phys., 141, 054310

Brooke J. S. A., Bernath P. F., Western C. M., 2015, J. Chem. Phys., 143, 026101

Campbell W. C., Tsikata E., Lu H. I., Van Buuren L. D., Doyle J. M., 2007, Phys. Rev. Lett., 98, 213001

Cernicharo J., Goicoechea J. R., Caux E., 2000, ApJ, 534, L199

Crawford I. A., Williams D. A., 1997, MNRAS, 291, L53

da Silva R. S., Alves M. D., Souza S. R., Fellows C., 2026, Spectrochim. Acta, Part A, 348, 127179

Darby-Lewis D. et al., 2019, J. Mol. Spectrosc., 362, 69

Draine B. T., 1978, ApJS, 36, 595

Fernando A. M., Bernath P. F., Hodges J. N., Masseron T., 2018, J. Quant. Spectrosc. Radiat. Transfer, 217, 29

Flores-Mijangos J., Brown J. M., Matsushima F., Odashima H., Takagi K., Zink L. R., Evenson K. M., 2004, J. Mol. Spectrosc., 225, 189

Geller M., Farmer C. B., Norton R. H., Sauval A. J., Grevesse N., 1991, A&A, 249, 550

Ghosh R., Choudhury B. S., Mezei J. Z., Schneider I. F., Pop N., Chakrabarti K., 2025, Phys. Chem. Chem. Phys., 27, 13021

Gilles A., Masanet J., Vermeil C., 1974, Chem. Phys. Lett., 25, 346

Glarborg P., Miller J. A., Ruscic B., Klippenstein S. J., 2018, Prog. Energy Combust. Sci., 67, 31

Graham W. R. M., Lew H., 1978, Can. J. Phys., 56, 85

Grevesse N., Lambert D. L., Sauval A. J., van Dishoeck E. F., Farmer C. B., Norton R. H., 1990, A&A, 232, 225

Hack W., Mill T., 1990, J. Mol. Spectrosc., 144, 358

Hall J. L., Adams H., Kasper J. V. V., Curl R. F., Tittel F. K., 1985, J. Opt. Soc. Am. B, 2, 781

Hamdan A., Liu J.-L., Cha M. S., 2018, Plasma Chem. Plasma Process., 38, 1003

Hanten E. B., Rousselot P., Jehin E., Hardy P., Hutsemékers D., Manfroid J., 2025, A&A, 702, A257

Harilal S. S., Brumfield B. E., Phillips M. C., 2018, Phys. Plasmas, 25, 083303

Hazi A. U., Taylor H. S., 1970, Phys. Rev. A, 1, 1109

Heays A. N., Bosman A. D., van Dishoeck E. F., 2017, A&A, 602, A105

Henderson R. D. E., Shayesteh A., Tao J., Haugen C. C., Bernath P. F., Le Roy R. J., 2013, J. Phys. Chem. A, 117, 13373

Hily-Blant P. et al., 2010, A&A, 521, L52

Hrodmarsson H. R., van Dishoeck E. F., 2023, A&A, 675, A25

Huber K. P., Herzberg G., 1979, Molecular Spectra and Molecular Structure IV. Constants of Diatomic Molecules. Van Nostrand Reinhold Company, New York

Janssen L. M. C., van der Avoird A., Groenenboom G. C., 2013, Phys. Rev. Lett., 110, 063201

Jin B., Deng Y., Li G., Li H., 2022, Int. J. Hydrogen Energy, 47, 36046

Kajita M., 2006, Phys. Rev. A, 74, 032710

Kirby K. P., Goldfield E. M., 1991, J. Chem. Phys., 94, 1271

Klaus T., Takano S., Winnewisser G., 1997, A&A, 322, L1

Lambert D. L., Brown J. A., Hinkle K. H., Johnson H. R., 1984, ApJ, 284, 223

Lamoureux N., Gasnot L., Desgroux P., 2019, Proc. Combust. Inst., 37, 1313

Le Roy R. J., 1999, J. Mol. Spectrosc., 194, 189

Le Roy R. J., Huang Y., 2002, J. Mol. Struct.: THEOCHEM, 591, 175

Leopold K. R., Evenson K. M., Brown J. M., 1986, J. Chem. Phys., 85, 324

Lewen F., Brünken S., Winnewisser G., Šimečková M., Štěpán U., 2004, J. Mol. Spectrosc., 226, 113

Li D., Bian W., 2021, Front. Chem., 9, 1

Mandelshtam V. A., Ravuri T. R., Taylor H. S., 1993, Phys. Rev. Lett., 70, 1932

Masanet J., Gilles A., Vermeil C., 1974, J. Photochem., 3, 417

Mashruk S., Alnasif A., Yu C., Thatcher J., Rudman J., Peronski L., Meng-Choung C., Valera-Medina A., 2023, J. Ammon. Energy, 1, 21

McKemmish L. K., 2021, WIREs Comput. Mol. Sci., 11, e1520

McKemmish L. K., Bowesman C. A., Kefala K., Perri A. N., Syme A. M., Yurchenko S. N., Tennyson J., 2024, RAS Tech. Instrum., 3, 565

Medvedev E. S., Ushakov V. G., 2022, J. Quant. Spectrosc. Radiat. Transfer, 288, 108255

Melosso M., Bizzocchi L., Tamassia F., Degli Esposti C., Canè E., Dore L., 2019, Phys. Chem. Chem. Phys., 21, 3564

Meyer D. M., Roth K. C., 1991, ApJ, 376, L49
Mitev G. B., Yurchenko S. N., Tennyson J., 2024, J. Chem. Phys., 160, 144110
Mitev G. B., Pezzella M., Bowesman C. A., Zhang J., Yurchenko S. N., Tennyson J., 2025, MNRAS, 539, 3732
Ni Q.-H., Hill C., Yurchenko S. N., Pezzella M., Fateev A. Z., Qin Z., Venot O., Tennyson J., 2025, RAS Tech. Instrum., 4, rzaf020
Patel-Misra D., Parlant G., Sauder D. G., Yarkony D. R., Dagdigian P. J., 1991, J. Chem. Phys., 94, 1913
Pattillo R. J., Cieszewski R., Stancil P. C., Forrey R. C., Babb J. F., McCann J. F., McLaughlin B. M., 2018, ApJ, 858, 10
Perri A. N., McKemmish L. K., 2024, MNRAS, 531, 3023
Persson C. M. et al., 2010, A&A, 521, L45
Persson C. M. et al., 2012, A&A, 543, A145
Pezzella M., Yurchenko S. N., Tennyson J., 2021, Phys. Chem. Chem. Phys., 23, 16390
Pezzella M., Yurchenko S. N., Tennyson J., 2022, MNRAS, 514, 4413
Pflieger R., Ouerhani T., Belmonte T., Nikitenko S. I., 2017, Phys. Chem. Chem. Phys., 19, 26272
Plomp V., Gao Z., Cremers T., van de Meerakker S. Y. T., 2019, Phys. Rev. A, 99, 033417
Ram R. S., Bernath P. F., 1986, J. Opt. Soc. Am. B, 3, 1170
Ram R. S., Bernath P. F., 2010, J. Mol. Spectrosc., 260, 115
Ram R. S., Bernath P. F., Hinkle K. H., 1999, J. Chem. Phys., 110, 5557
Ramsay D. A., Sarre P. J., 1982, J. Mol. Spectrosc., 93, 445
Robinson A., Brown J., Jesus Flores-Mijangos L. Z., Jackson M., 2007, Mol. Phys., 105, 639
Smith V. V., Lambert D. L., 1986, ApJ, 311, 843
Smith W. H., Brzozowski J., Erman P., 1976, J. Chem. Phys., 64, 4628
Sneden C., 1973, ApJ, 184, 839
Sokolov A., Brady R. P., Yurchenko S. N., Tennyson J., 2025, MNRAS, 543, 1435
Sokolov A., Yurchenko S. N., Tennyson J., 2026, Phys. Chem. Chem. Phys., 28, 7484
Spite M., Spite F. Caffau E., Bonifacio P. François P., 2022, A&A, 667, A139
Swings P., Elvey C. T., Babcock H. W., 1941, ApJ, 94, 320
Tennyson J., Pezzella M., Zhang J., Yurchenko S. N., 2023, RAS Tech. Instrum., 2, 231
Tennyson J. et al., 2024, J. Quant. Spectrosc. Radiat. Transf., 326, 109083
Ubachs W., Meyer G., ter Meulen J. J., Dymanus A., 1986, J. Mol. Spectrosc., 115, 88
Uhlíková T., Yurchenko S. N., Perri A. N., Tennyson J., Kim G.-S., 2025, J. Chem. Phys., 162, 144108
van den Heuvel F., Meerts W., Dymanus A., 1982, Chem. Phys. Lett., 92, 215
van Dishoeck E. F., Black J. H., 1982, ApJ, 258, 533
van de Meerakker S. Y. T., Sartakov B. G., Mosk A. P., Jongma R. T., Meijer G., 2003, Phys. Rev. A, 68, 032508
van de Meerakker S. Y. T., Labazan I., Hoekstra S., Küpper J., Meijer G., 2006, J. Phys. B: Atom. Mol. Opt. Phys., 39, S1077
Weselak T., Galazutdinov G. A., Beletsky Y., Krelowski J., 2009, MNRAS, 400, 392
Yan N.-Z., Yang C.-L., Sun Z.-P., Wang M.-S., Ma X.-G., 2021, Spectrochim. Acta, Part A, 250, 119229
Yurchenko S. N., Lodi L., Tennyson J., Stolyarov A. V., 2016, Comput. Phys. Commun., 202, 262
Yurchenko S. N., Al-Refaie A. F., Tennyson J., 2018, A&A, 614, A131
Yurchenko S. N., Szajna W., Hakalla R., Semenov M., ov A., Tennyson J., Pavlenko Y., Schmidt M. R., 2024, MNRAS, 527, 9736
Zhang D., Gao Q., Li B., Liu J., Li Z., 2019, Appl. Opt., 58, 1210

SUPPORTING INFORMATION

Supplementary data are available at *MNRAS* online.

14N-1H__2kNigHt.model

This paper has been typeset from a TEX/LATEX file prepared by the author.